Research Square

Preprints are preliminary reports that have not undergone peer review.
They should not be considered conclusive, used to inform clinical practice,
or referenced by the media as validated information.

Effects of In and Ni on the Microstructure and Micro Joint Properties of Sn20Bi Solder Balls Prepared by the Pulsated Orifice Ejection Method

Fumin Xu
Dalian University of Technology
Xiangxiang Zhang
Dalian University of Technology
Donghang Liu
Dalian University of Technology
Wei Dong
w-dong@dlut.edu.cn

Dalian University of Technology

Research Article

Keywords: Lead-free solder, Sn-Bi alloy, Pulsated orifice ejection method, Microalloying, Interfacial reaction

Posted Date: November 24th, 2026

DOI: https://doi.org/10.21203/rs.3.rs-11609057/v1

License: This work is licensed under a Creative Commons Attribution 4.0 International License.
Read Full License

Additional Declarations: No competing interests reported.

Effects of In and Ni on the Microstructure and Micro Joint Properties of Sn20Bi Solder Balls Prepared by the Pulsated Orifice Ejection Method

Fumin Xu [a], Xiangxiang Zhang [a], Donghang Liu [a], Wei Dong [a*]

a.School of Materials Science and Engineering, Dalian University of Technology, Dalian 116024, China

**Corresponding authors, E-mail addresses:*

w-dong@dlut.edu.cn (Wei Dong)

ABSTRACT:

Sn-Bi-based solders possess advantages such as a low melting point, lead-free and environmentally friendly nature, and relatively low cost, showing application potential in temperature-sensitive electronic packaging and low-temperature soldering fields. In this study, 200 μm Sn20Bi, Sn20Bi-xIn, and Sn20Bi-0.4Ni-xIn alloy solder balls were successfully fabricated by the Pulsated Orifice Ejection Method (POEM). The effects of In/Ni microalloying on their microstructure and micro joint properties were systematically investigated. The In/Ni-microalloyed solder balls retained good sphericity and a narrow particle size distribution. In/Ni addition suppressed coarsening and local enrichment of the Bi phase, refined the β-Sn grains, , and modified the grain boundary characteristics and KAM distribution. The wettability of the solder joints was improved, with a minimum contact angle of 22.54° and a maximum shear strength of 70.42 MPa. The results indicate that In/Ni microalloying overall improved the microstructure, interfacial structure, and joint wettability and shear properties of Sn20Bi solder balls prepared by POEM, providing an experimental basis for their application in temperature-sensitive electronic packaging interconnections.

Keywords：Lead-free solder; Sn-Bi alloy; Pulsated orifice ejection method; Microalloying; Interfacial reaction

1.Introduction

With the continuous development of electronic products toward miniaturization, high integration, and multifunctionality, electronic packaging technology plays a critical role in establishing electrical connections, providing mechanical support, and enabling thermal management between chips and substrates [1]. The packaging interconnection structure not only determines the electrical conductivity of the device but also affects its thermomechanical reliability during service. In particular, under thermal cycling, mechanical shock, and thermal expansion coefficient mismatch, solder joints often become the weak link in electronic device failure. Among various packaging forms, Ball Grid Array (BGA) packaging has been widely used in the packaging of integrated circuits and high-performance electronic devices due to its high interconnection density, controllable solder joint pitch, and high packaging area utilization [2]. Ball Grid Array (BGA) packaging achieves electrical and mechanical connections between the chip package and the printed circuit board through regularly arranged solder balls. Therefore, solder balls serve not only as conductive channels but also as critical structural units bearing thermomechanical stresses. For BGA packaging, the melting characteristics, wetting and spreading ability, interfacial intermetallic compound (IMC) growth behavior, and mechanical properties of solder joints of the solder ball material all affect the reliability of packaging interconnections.

Conventional Sn-Pb solders were long used in electronic packaging interconnections owing to their low melting point, good wettability, and mature processing technology. However, Pb poses environmental and health hazards, and the electronics manufacturing industry has gradually been subject to regulations restricting hazardous substances. Consequently, the development of environmentally friendly lead-free solders has become an important research direction in electronic packaging materials [3]. Currently, the Sn-Ag-Cu solder system is one of the most commonly used lead-free solder systems. However, its relatively high reflow temperature may increase the risks of substrate warpage, thermal damage to devices, and thermal mismatch stress in temperature-sensitive devices, flexible substrates, and high-density packaging. Therefore, low-to-medium temperature lead-free solders have gradually become an important research direction in advanced electronic packaging.

Owing to their relatively low melting point and low cost, Sn-Bi-based solders are regarded as a lead-free solder system with promising application potential [4-6]. Although eutectic Sn-58Bi solder possesses a relatively low melting point, its high Bi content results in a high fraction of Bi-rich phase, which may lead to coarsening of this phase and increased brittleness of solder joints, thereby adversely affecting the mechanical properties of the joints [7]. By comparison, Sn20Bi exhibits a relatively high tensile strength among non-eutectic systems [8], and it falls within the same reflow temperature range as Sn-Pb, thereby reducing the Bi phase content while maintaining a relatively low melting temperature and providing greater compositional design space for subsequent microalloying-mediated regulation of the microstructure and interfacial reactions.

However, during solidification and reflow, Sn20Bi solder may still be susceptible to local coarsening of the Bi phase, insufficient wetting and spreading, and non-uniform growth of the IMC layer [8], which may affect the metallurgical bonding between BGA solder balls and pads as well as the shear properties of solder joints. Microalloying is an effective approach for improving the microstructure and properties of Sn-Bi-based solders [9]. As a low-melting-point metal, In can lower the melting temperature of solder and improve wettability [10], while also regulating the

microstructure and distribution of the Bi phase, thereby affecting local stress concentration and mechanical properties. Previous studies [11-13] have shown that In addition decreases the DSC peak temperature and affects the wetting behavior of Sn-Bi solder on Cu substrates; Ni can form a Ni_3Sn_4 second phase with Sn and further influence the solidification microstructure and interfacial IMC growth behavior. An appropriate amount of Ni_3Sn_4 second phase can serve as heterogeneous nucleation sites, promote the refinement of the solidification microstructure, and affect the mechanical properties of the solder through mechanisms such as second-phase strengthening. Previous studies [14-16] have shown that Ni addition can improve the microstructure, wettability, and mechanical properties of Sn-Bi solders. Therefore, introducing In and Ni into the Sn20Bi matrix is expected to regulate the solder properties in terms of wetting behavior, microstructural evolution, and interfacial reactions.

Currently, solder ball preparation methods mainly include atomization, wire cutting andremelting, and solder paste printing. The conventional atomization method offers high output, but the resulting solder balls exhibit a wide particle size distribution, usually requiring subsequent sieving, and it is difficult to precisely control the sphericity and size consistency of small-sized solder balls [17]. The wire cutting and remelting method is relatively simple in process, but it strongly depends on wire dimensions, cutting precision, and remelting conditions, suffering from problems such as a long process flow, low efficiency, dimensional deviation, and non-uniform sphericity [18]. The solder paste printing method is susceptible to the influence of stencil precision, solder paste performance, and reflow conditions, which may result in poor consistency in solder joint size and morphology [19]. Therefore, it is necessary to develop a solder ball preparation process that simultaneously achieves high sphericity, a narrow particle size distribution, and microstructural homogeneity. Droplet printing technology has promising application potential in the field of advanced packaging [20]. Among these methods, the Pulsated Orifice Ejection Method (POEM) is a droplet ejection preparation technology used for fabricating spherical metal particles. POEM enables the controlled generation of monodisperse spherical droplets through pulse actuation, enabling precise regulation of particle sizes ranging from tens to hundreds of micrometers, and yielding metal particles with relatively high sphericity and a narrow particle size distribution [21-24].

Based on the above design rationale, in this study, Sn20Bi, Sn20Bi-xIn, and Sn20Bi-0.4Ni-xIn solder balls were prepared by the POEM preocess, and the effects of In and Ni on the microstructure and properties of the solder balls were systematically investigated. The melting behavior of the solders was analyzed by DSC, and the phase composition was identified by XRD. Combined with surface SEM, cross-sectional SEM, and EDS mapping, the surface morphology and cross-sectional microstructure of the solder balls were observed. The grain orientation, grain boundary characteristics, and KAM distribution within the solder matrix were investigated by EBSD. Furthermore, their wetting behavior and shear resistance were evaluated by wettability and shear strength tests.

2.Materials and Methods

Solder balls were prepared using POEM, and the working principle of the experimental apparatus is schematically illustrated in Fig. 1. The apparatus operates by first melting the solder alloy. A piezoelectric ceramic then drives the transmission rod through the molten alloy to generate a pulsed pressure wave. When the pressure wave propagates to the orifice and the sum of the pulsed

pressure and the static pressure of the melt exceeds the Laplace force generated by surface tension at the orifice [22], a certain amount of molten metal or alloy is ejected from the orifice to form a droplet (step 1). During flight, the droplet gradually tends to become spherical under the action of surface tension and rapidly solidifies into a microsphere during cooling (step 2). The schematic diagram of the pulse waveform is shown in Fig. 1, which is specifically divided into three stages: rising edge, holding edge, and falling edge. The voltage is controlled at 3 to7 V, and the rising edge time ranges from 50 to 300 μs. In this experiment, high-purity Sn, high-purity Bi, high-purity In (all with a purity of 99.99%), and a Sn-0.5 wt% Ni master alloy were used as raw materials. The nominal compositions of the alloys were Sn20Bi-xIn (x = 0, 0.5, 1, 1.5, 2 wt%) and Sn20Bi-0.4Ni-xIn (x = 0.5, 1, 1.5, 2 wt%), and the composition ratios are listed in Table 1. The Ni element was added in the form of a Sn-0.5 wt% Ni master alloy. According to the nominal composition conversion, the actual addition amount of Ni calculated from the master alloy ratio is approximately 0.39 wt%. For convenience of description, the nominal composition of 0.4Ni is uniformly used for identification in the text and figures. Before the experiment, a crucible with a corresponding orifice diameter at the bottom center should be selected according to the target solder ball size, and approximately 30 g of solder was placed into the crucible. The target solder ball diameter in this experiment was 200 μm. Based on previous research results [22], a crucible with an orifice diameter of 300 μm was selected. After loading, to avoid interference from oxygen and other gas impurities on the experimental results, the vacuum chamber must be subjected to evacuation and Ar backfilling cycles before heating. First, the vacuum chamber was evacuated to 4.5×10^{-3} Pa, and then high-purity (≥99.9999%) Ar was backfilled to atmospheric pressure. The above evacuation and Ar backfilling process was repeated three times. The alloy was heated to 450 °C and held for 20 min to ensure complete melting of the alloy. A micrometer adjuster with a control precision of 0.01 mm was used to adjust the distance between the transmission rod and the orifice, thereby obtaining droplets with stable size and narrow distribution.

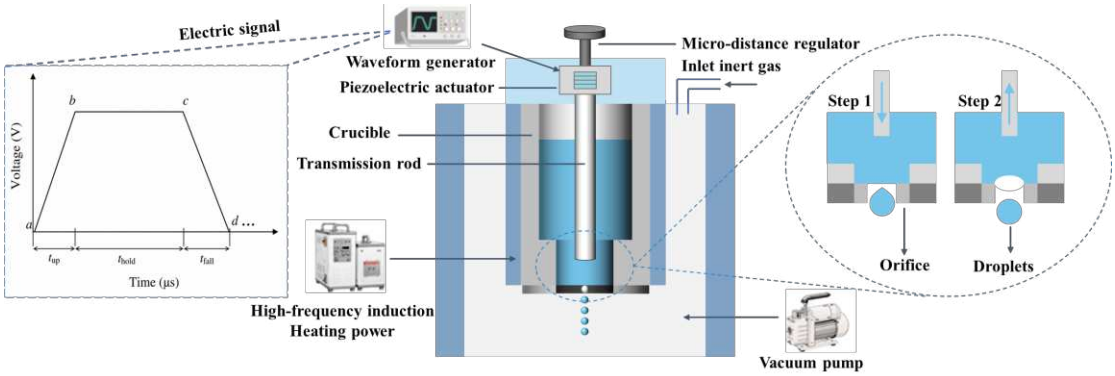


Fig. 1. Schematic illustration of the working principle of the POEM equipment.

Table 1 Chemical composition of the alloys (wt.%)

Alloy	Sn	Sn-0.5wt.%Ni	Bi	In
Sn20Bi	80	—	20	—
Sn20Bi-xIn	79.5，79，78.5，78	—	20	0.5，1，1.5，2

Sn20Bi-0.4Ni-xIn	—	79.5，79，78.5，78	20	0.5，1，1.5，2

An Olympus optical microscope (LV100NPOL, Japan) equipped with a bottom light source was used to collect contour images of the solder balls, and image analysis software (WinRoof 2018, Mitani Corp.) was used to determine the particle size distribution and sphericity of the prepared solder balls. Phase analysis was performed using an X-ray diffractometer (Empyrean, Netherlands) with Cu Kα radiation (λ = 0.15406 nm) operated at 40 kV and 30 mA. The melting behavior and characteristic temperatures of the solder balls were analyzed by a thermogravimetric-differential scanning calorimeter (TG-DSC, Mettler Toledo) under an argon atmosphere in the range of 50–250 °C at a heating rate of 10 °C/min. The melting enthalpy of the samples was calculated from the integrated area of the endothermic peak. The morphology of the solder balls was observed using a field-emission scanning electron microscope (SU5000, Japan), and the elemental distribution of the solder balls was analyzed by an energy-dispersive spectrometer (EDS). EBSD was used to investigate the grain orientation, crystallographic characteristics, and KAM distribution of the solder matrix. The substrate used for soldering was an FR-4 substrate with Cu pads treated by OSP on the surface. The pad diameter was 150 μm, and the substrate size was 1 cm × 1 cm. The approximate structure of the substrate is shown in Fig. 2(a). Before the reflow soldering experiment, G95 no-clean flux paste was coated on the substrate, and then reflow soldering was performed in a vacuum reflow furnace with N_2 as the protective atmosphere. Both the heating and cooling rates were 1 °C/s, and the temperature profile during reflow is shown in Fig. 2(b). A ball shear tester (STELLAR 4000PLUS) was used to evaluate the shear strength of the solder joints, with a shear height of 50 μm and a shear speed of 100 μm/s. The ball shear test is shown in Fig. 2(c). Pure Cu substrates were used for the wetting experiments, and a constant-temperature hot plate (HPA-2020, China) was used with the temperature set at 220 °C. An optical contact angle goniometer (SDC-350, China) was used to measure the contact angle of the solder on the Cu substrate. The equivalent thickness of the IMC layer was analyzed by ImageJ, and the ratio of the IMC area along the measured interfacial region to the corresponding interfacial length was taken as the equivalent average thickness.

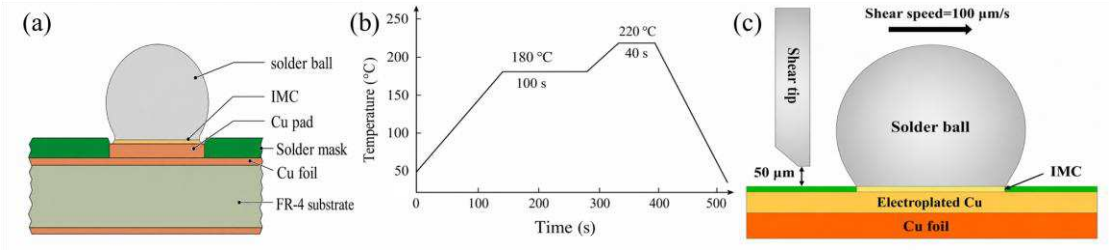


Fig. 2 Schematic illustration of the soldering process and ball shear test: (a) schematic diagram of the substrate structure; (b) reflow temperature profile; (c) schematic diagram of the ball shear test.

3.Results and Discussion

3.1 Forming Quality and Surface Morphology Evolution of Solder Balls

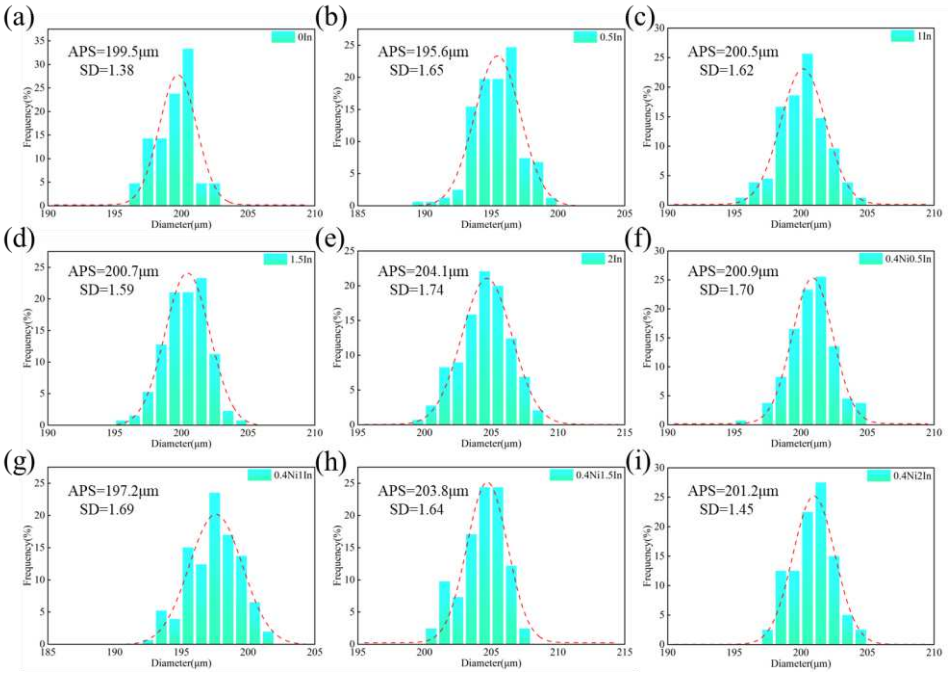


Fig. 3 Particle size distributions of solder balls with different compositions.(APS: average particle size; SD: standard deviation)

The size of solder balls prepared by the POEM process is jointly affected by parameters such as the rising edge time (tup), piezoelectric ceramic driving voltage, rod distance, and orifice diameter. The solder ball size is positively correlated with the driving voltage and negatively correlated with the rising edge time [24]. Fig. 3 shows the particle size distributions of monodisperse Sn20Bi-xIn (x = 0, 0.5 wt%, 1 wt%, 1.5 wt%, 2 wt%) and Sn20Bi-0.4Ni-xIn (x = 0.5 wt%, 1 wt%, 1.5 wt%, 2 wt%) solder balls prepared under an Ar atmosphere. It can be seen that the particle sizes of the solder balls in each group are close to the target value of 200 μm, and the particle size distributions are relatively concentrated. This indicates that the POEM process can directly produce solder balls with relatively concentrated particle size distributions without additional sieving, and also indicates that microalloying did not significantly affect the particle size consistency of the solder balls. Fig. 4 presents the quantitative analysis results of nine groups of solder balls. The results show that the solder balls have highly rounded two-dimensional contours, further indicating that POEM is suitable for preparing micron-sized solder balls with relatively high sphericity. In the Sn20Bi-xIn series, the sphericity of the solder balls generally increases with increasing In content. For the Sn20Bi-0.4Ni-xIn series, the sphericity fluctuates to some extent with different In contents, but all groups still maintain a relatively high level, indicating that microalloying did not obviously deteriorate the formability of the solder balls. For BGA packaging, high sphericity and a concentrated particle size distribution can improve the stability of the placement and reflow processes and ensure consistency in solder joint height, load, and thermal response, thereby facilitating the formation of interconnection solder joints with stable morphology and reliable metallurgical bonding. This is an important prerequisite for ensuring packaging quality and long-term reliability [25].

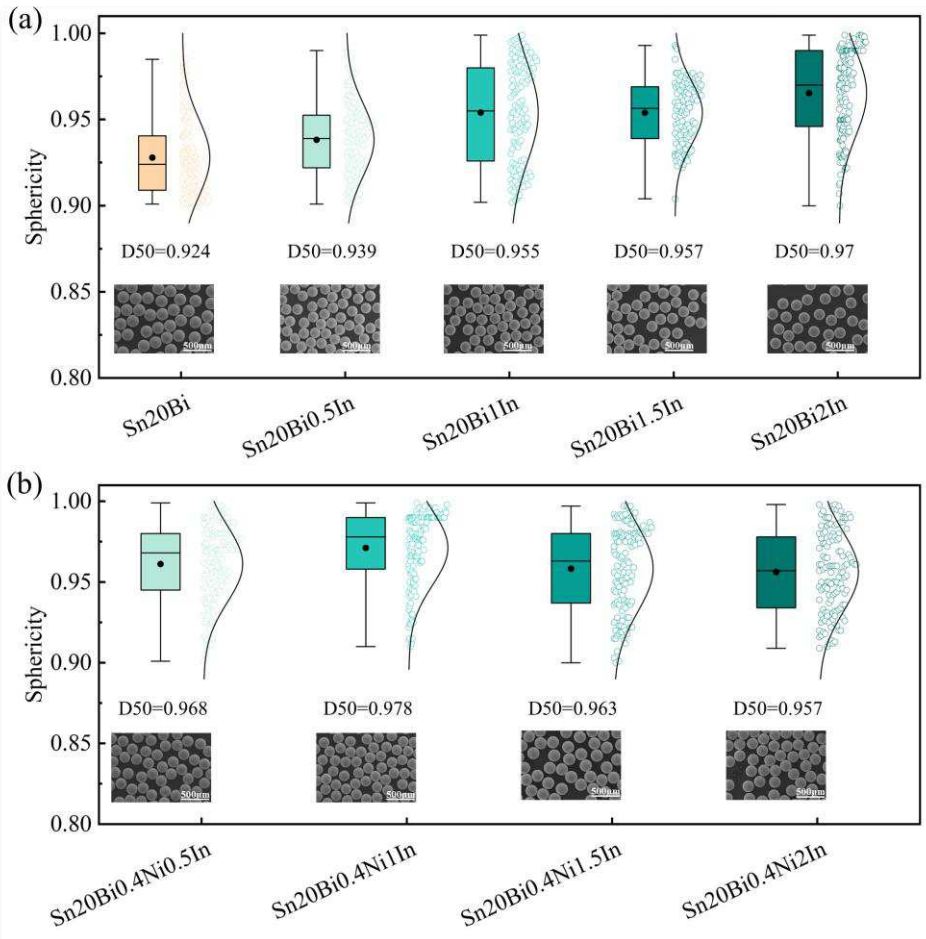


Fig. 4 Box plots of sphericity distribution for (a) Sn20Bi-xIn (x = 0, 0.5, 1, 1.5, 2 wt%) and (b) Sn20Bi-0.4Ni-xIn (x = 0.5, 1, 1.5, 2 wt%) solder balls.

Fig. 5 shows the SEM images of the surface morphology of Sn20Bi, Sn20Bi-xIn, and Sn20Bi-0.4Ni-xIn solder balls prepared by the POEM process. The SEM images show that the prepared solder balls are generally regular spheres with clear boundaries and relatively smooth and dense surfaces. No satellite powders, obvious rupture or collapse, or severe agglomeration were observed, indicating that the POEM process has good ball-forming capability.

After microalloying, the solder balls in each group still maintained a relatively good spherical morphology, with no severe agglomeration or large-sized pores, indicating that the addition of a small amount of In and Ni did not have an obvious adverse effect on the ball-forming capability of the solder balls. As shown in Fig. 5(a), the surface of the Sn20Bi solder balls exhibits a relatively obvious dendritic morphology. In contrast, the surfaces of the In-added Sn20Bi-xIn solder balls are overall smoother and denser, with only a small amount of fine solidification textures remaining. From Fig. 5(b)–(e), as the In content increases, the solder ball surfaces generally exhibit a smoother and more uniform morphological characteristic. This change in surface morphology may be related to In altering the melt surface tension and regulating interfacial behavior, thereby affecting the morphological evolution of the droplets during flight and solidification [13].

For the Sn20Bi-0.4Ni-xIn solder balls with further Ni addition, according to the EDS mapping results, no obvious Ni-enriched regions or local agglomeration were observed on the solder ball

surfaces. The role of Ni may be related to the evolution of the solidification microstructure and changes in microstructural scale [26], and its specific effect will be discussed in the subsequent microstructural analysis.

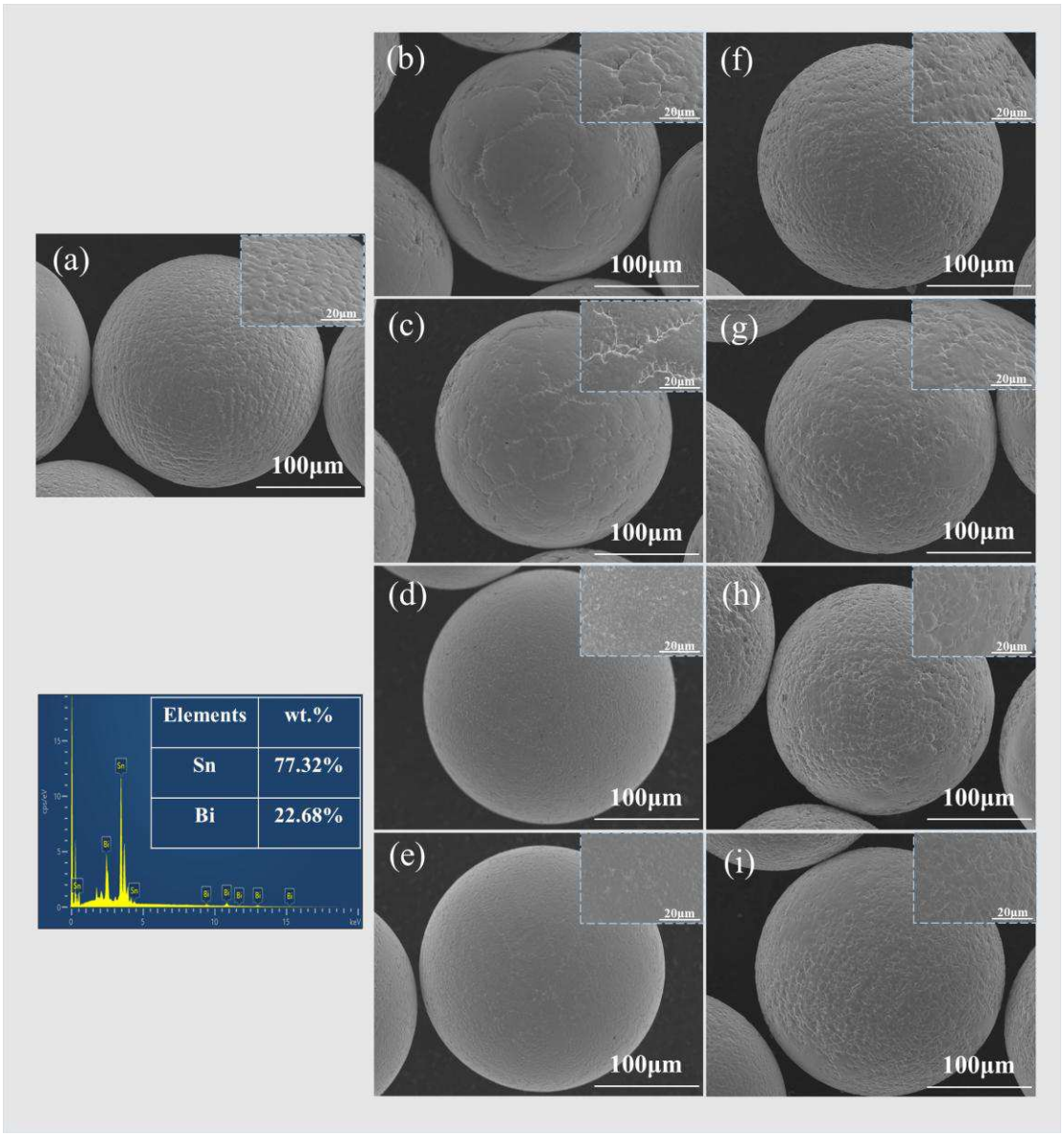


Fig. 5 Surface morphologies of solder balls with different compositions: (a) surface morphology of Sn20Bi solder balls; (b–e) surface morphologies of Sn20Bi-xIn (x = 0.5–2 wt.%) solder balls; (f–i) surface morphologies of Sn20Bi-0.4Ni-xIn (x = 0.5–2 wt.%) solder balls.

3.2 Phase Composition and Melting Behavior Analysis

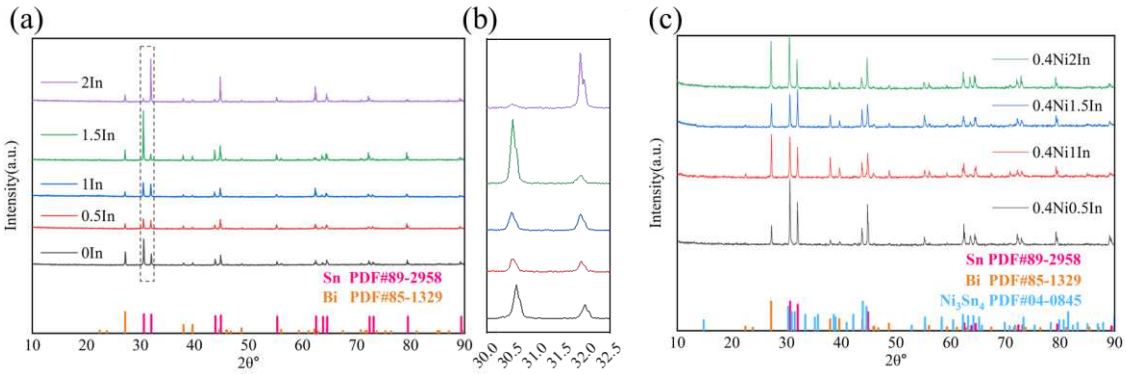


Fig. 6 (a) XRD patterns of Sn20Bi-xIn; (b) magnified view of the 30°–32.5° region in (a); (c) XRD patterns of Sn20Bi-0.4Ni-xIn.

Fig. 6(a) and (c) show the XRD patterns of Sn20Bi-xIn (x = 0–2 wt.%) and Sn20Bi-0.4Ni-xIn (x = 0.5–2 wt.%), respectively. According to the XRD pattern analysis, the Sn20Bi solder balls contain two phases: a body-centered tetragonal β-Sn phase and a rhombohedral Bi phase. After the addition of In, no obvious independent diffraction peaks of an In phase were observed, which may be because the In content is relatively low and most of it is dissolved in the Sn matrix [13]. For the Ni-containing alloys, diffraction peaks of the Ni_3Sn_4 phase appear in the patterns. Therefore, the XRD analysis results indicate that the main crystalline phases detected are β-Sn, Bi, and Ni_3Sn_4 in the Ni-containing samples, with no obvious impurity phases or oxide phases. Fig. 6(b) is a magnified view of the 30°–32.5° region in Fig. 6(a). It can be seen that the Sn diffraction peaks shift overall toward lower angles, with a maximum shift of 0.475°. According to the Bragg equation

$$2d\sin\theta = n\lambda \quad (1)$$

where, d is the interplanar spacing, θ is the diffraction angle, λ is the X-ray wavelength, and n is the diffraction order, which is usually taken as 1. A shift of the diffraction peak to a lower angle indicates an increase in the interplanar spacing of the corresponding crystal plane. Therefore, the addition of In may cause lattice distortion or changes in the lattice parameters of the β-Sn phase [27], which is consistent with the possible phenomenon that In enters the β-Sn matrix and induces changes in the lattice state [1,13]. This result indicates that the addition of In may not only affect the phase composition of the solder balls but also alter the crystal structure state of the β-Sn phase. In summary, the XRD results indicate that the addition of In is related to changes in the lattice state of β-Sn, while the addition of Ni is accompanied by the formation of the Ni_3Sn_4 phase, providing a phase basis for the subsequent analysis of the effects of In/Ni on microstructural evolution.

The melting characteristics of solder directly affect its processing temperature range and soldering process applicability, and also influence the thermal process during soldering and joint formation. DSC was used to analyze the melting behavior of Sn20Bi-based solder balls with different compositions, and the results are shown in Fig. 7(a) and (c). Each DSC curve exhibits two endothermic peaks. Considering the overall composition of Sn20Bi as a Sn-rich non-eutectic alloy and the redistribution of solute Bi during rapid solidification in POEM, β-Sn preferentially forms and may promote the enrichment of Bi in the remaining liquid phase. The locally Bi-rich remaining liquid phase may reach the conditions for eutectic-type transformation. Therefore, the low-temperature endothermic peak is related to the preferential melting of these low-melting-point regions, followed by further melting of β-Sn and the formation of the high-temperature endothermic

peak. The onset temperature of the second endothermic peak is defined as the characteristic melting temperature T_m, and the endpoint temperature of the second endothermic peak is defined as the melting end temperature T_n. The melting range of the solder is expressed as the difference between the melting end temperature and the characteristic melting temperature.

As shown in Fig. 7(a) and (c), after In addition, the endothermic peaks of the solder balls shifted toward lower temperatures overall, indicating that the addition of In shifted T_m and the endothermic peak temperatures toward lower temperatures overall. Under the same reflow temperature conditions, a lower T_m may facilitate the solder to enter a fully liquid state earlier, thereby improving its spreading process. Fig. 7(b) and (d) show the T_m and T_n values of the nine solder balls, respectively. The melting ranges corresponding to the nine groups of solder balls are 16.3 °C, 19.8 °C, 20 °C, 21.2 °C, 21.2 °C, 13.9 °C, 26.3 °C, 25 °C, and 19.8 °C, respectively.

In the Sn20Bi-xIn series, the melting range gradually increased from 16.3 °C to 21.2 °C, indicating that the addition of In mainly shifted the characteristic melting temperature toward lower temperatures without narrowing the melting temperature interval of the solder balls. Combined with the staged melting characteristics of the non-eutectic Sn20Bi system, its melting behavior exhibits a certain temperature span. Although the melting range was not significantly shortened, under the same reflow conditions, a lower characteristic melting temperature implies that the solder may have a greater liquid temperature margin, which is beneficial for spreading and flow.

In the Sn20Bi-0.4Ni-xIn series, the characteristic melting temperature decreased from 190.8 ℃ to 180.6 ℃ with increasing In content, indicating that In retained its melting-point-depressing effect in the Ni-containing system. Compared with the Ni-free solders at the same In content, the Ni-containing samples exhibited characteristic melting temperatures approximately 3–6 ℃ higher, which may be associated with the formation of Ni_3Sn_4 and the resulting local microstructural changes, although its effect was smaller than that induced by the variation in In content within the investigated composition range [28].

In summary, within the scope of this study, the effect of In on the characteristic melting temperature is relatively pronounced; the Ni-containing samples form a Ni_3Sn_4 phase detectable by XRD, but its specific role in the melting behavior and microstructural evolution still requires further analysis.

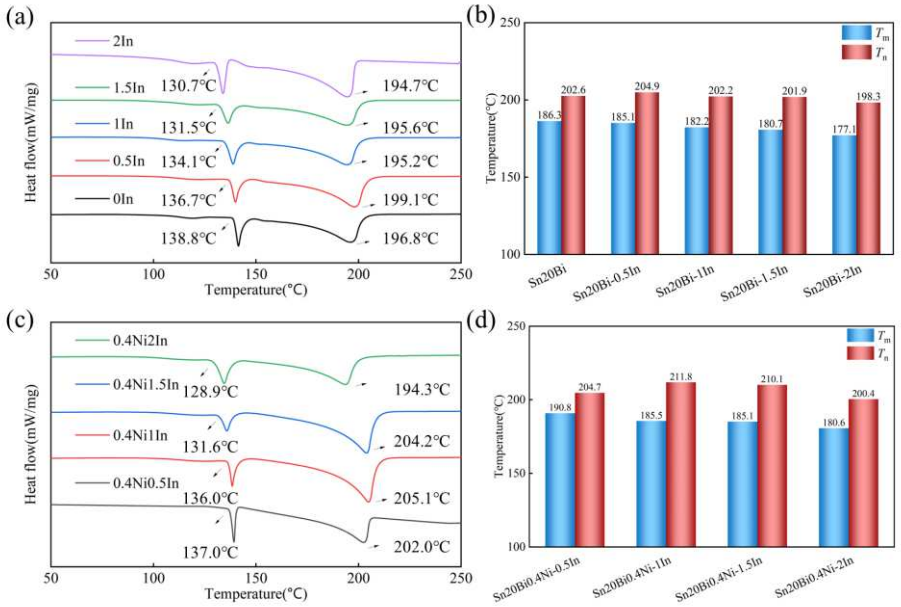


Fig. 7. DSC curves and solidus-liquidus temperatures of the solder balls: (a, b) Sn20Bi-xIn (x = 0–2 wt.%) compositions; (c, d) Sn20Bi-0.4Ni-xIn (x = 0.5–2 wt.%) compositions.

3.3 Temperature Field

During rapid solidification of the droplet, the transformation from liquid to solid releases latent heat of crystallization, which affects the temperature variation near the solid-liquid interface. Meanwhile, the liquid phase far from the solid-liquid interface remains at a relatively low temperature and in a certain undercooled state. Therefore, along the crystal growth direction from the solid-liquid interface toward the interior of the liquid phase ahead, a radial temperature distribution varying from a higher-temperature region to a lower-temperature region is formed within the droplet [16], This study discusses the temperature variation and spatial distribution within the droplet from the center to the surface. Such a temperature distribution may affect the solidification behavior and microstructural evolution of the droplet. Local heat transfer conditions, together with factors such as undercooling, interfacial kinetics, and thermophysical properties of the material, jointly affect the advancement of the solid-liquid interface and crystal growth. Studies have shown that the microstructural differences in different radial regions of the particle are related to the non-uniformity of its thermal history, local cooling rate, and temperature gradient [29,30]. Therefore, accurately describing and systematically analyzing the heat transfer behavior of the droplet during rapid solidification is an important basis for analyzing its solidification behavior and microstructural evolution.

In POEM, droplets complete flight, cooling, and solidification under containerless conditions [31]. During this process, the droplets fall freely in a protective atmosphere and exchange heat with the surrounding environment mainly through gas convective heat transfer and surface radiation. Owing to the small size of micron-sized droplets and their high cooling rate (up to the order of 10^4 K/s), it is experimentally difficult to directly obtain the transient temperature field inside the flying droplets. Therefore, numerical model-based heat transfer and solidification simulations can be used

to analyze the particle cooling path, temperature distribution, and solidification process.

By establishing a heat transfer-solidification coupled model in a three-dimensional spherical coordinate system, the temperature evolution and solidification progress inside the droplet under different cooling conditions can be simulated, providing a theoretical basis for analyzing the thermal history and solidification process of POEM-prepared droplets. The model and three-dimensional spherical coordinate system adopted in this study are described in Ref [32].Here, the heat transfer governing equation can be expressed as:

$$\frac{\partial}{\partial t}(\rho c_p T)=\frac{1}{r^2}\frac{\partial}{\partial r}\left(\lambda r^2\frac{\partial T}{\partial r}\right)+\frac{1}{r^2\sin^2\theta}\frac{\partial}{\partial \varphi}\left(\lambda\frac{\partial T}{\partial \varphi}\right)+\frac{1}{r^2\sin\theta}\frac{\partial}{\partial \theta}\left(\lambda\sin\theta\frac{\partial T}{\partial \theta}\right)+Q \tag{2}$$

where, ρ is the material density, c_p is the specific heat capacity, t is time, λ is the thermal conductivity, T is the temperature of the infinitesimal element, Q is the internal heat source within the particle, r, θ and φ are the radial distance, polar angle, and azimuthal angle in the model, respectively. During the calculation, the latent heat of solidification is treated as an internal heat source, and the equivalent specific heat method is adopted to handle the latent heat of solidification. In the solid-liquid two-phase region, the volumetric equivalent heat capacity C is expressed as:

$$C=\frac{\Delta H}{T_{\mathrm{L}}-T_{\mathrm{S}}}\times 10^{-3} \tag{3}$$

where, T_{L} and T_{S} are the liquidus and solidus temperatures, respectively, and ΔH is the latent heat of solidification, all determined by DSC.

The initial conditions for the calculation are set as follows: the initial temperature of the droplet upon ejection from the orifice is T_0=450 ℃, the chamber wall temperature is T_{w}=20℃, the argon gas temperature in the chamber is T_{g}=50℃, and the initial falling velocity of the droplet from the orifice is v_0=1 m/s [32]. Two heat transfer mechanisms exist on the droplet surface: one is heat exchange via radiation between the droplet surface and the chamber wall, and the other is convective heat transfer from the droplet surface to the argon gas.

$$q_{\mathrm{rad}}=\varepsilon\sigma\left(T_{\mathrm{s}}^4-T_{\mathrm{w}}^4\right) \tag{4}$$

$$q_{\mathrm{conv}}=-h\left(T_{\mathrm{s}}-T_{\mathrm{g}}\right) \tag{5}$$

where q_{rad} and q_{conv} are the heat flux densities generated by radiation and convection, respectively; ε is the emissivity, taken as 0.8 in this calculation, and is related to the shape of the object; σ is the Stefan–Boltzmann constant, taken as $5.67\times10^{-8}\ \mathrm{W\cdot m^{-2}\cdot K^{-4}}$, T_{s} is the particle surface temperature; h is the convective heat transfer coefficient, which depends on the velocity difference between the ambient gas and the droplet and follows the equation below:

$$h=\frac{k_{\mathrm{g}}}{d}\left(2.0+0.6\sqrt[3]{Pr}\sqrt{Re}\right) \tag{6}$$

where k_{g} is the thermal conductivity of the gas, d is the particle diameter, Re is the Reynolds number, $Re=\frac{\rho_{\mathrm{g}}dv_{\mathrm{m}}}{\mu_{\mathrm{g}}}$, Pr is the Prandtl number, $Pr=\frac{c_{pg}\mu_{\mathrm{g}}}{k_{\mathrm{g}}}$, v_{m} is the falling velocity of the droplet, ρ_{g} is the gas density, μ_{g} is the dynamic viscosity of the gas, and c_{pg} is the specific heat capacity of the gas. In this study, the gas used was argon.

During the falling process of the droplet, the effects of its own gravity, gas buoyancy, and gas

drag need to be considered. Therefore, the instantaneous velocity of the droplet during falling satisfies the following dynamic equation:

$$m_{\mathrm{d}}\frac{\mathrm{d}v_{\mathrm{t}}}{\mathrm{d}t}=m_{\mathrm{d}}g-\rho_{\mathrm{g}}V_{\mathrm{d}}g-\frac{1}{2}C_{D}\rho_{\mathrm{g}}A_{\mathrm{d}}v_{\mathrm{t}}^{2} \tag{7}$$

where $m_{\mathrm{d}}g$ is the gravitational force of the droplet, $\rho_{\mathrm{g}}V_{\mathrm{d}}g$ is the gas buoyancy, $\frac{1}{2}C_{\mathrm{D}}\rho_{\mathrm{g}}A_{\mathrm{d}}v_{\mathrm{t}}^{2}$ is the gas drag force, m_{d} is the droplet mass, v_{t} is the instantaneous velocity of the droplet, t is the falling time of the droplet, $\frac{\mathrm{d}v_{\mathrm{t}}}{\mathrm{d}t}$ is the instantaneous acceleration of the droplet, g is the gravitational acceleration, usually taken as 9.81 m/s^2, V_{d} is the droplet volume, A_{d} is the frontal projected area of the droplet along the direction of motion, and C_{D} is the gas drag coefficient, which can be calculated by the following equation:

$$C_{D}=0.28+\frac{6}{\sqrt{Re}}+\frac{21}{Re} \tag{8}$$

In this study, the explicit finite difference scheme was adopted to discretize the heat transfer governing equation [33].

The temperature field simulation was performed for Sn20Bi microspheres, while the cooling rate calculation and solidification process analysis were conducted for Sn20Bi-xIn (x = 0, 1, 2 wt.%). Argon was used as the inert gas atmosphere, and the physical parameters are listed in Table 2.

Table 2 Thermophysical properties for solidification simulations.

Parameter/unit	Nomenclature	Value
$k_{\mathrm{g}}/\mathrm{W\cdot m^{-1}\cdot K^{-1}}$	Ar thermal conductivity	1.763×10^{-2}
$\rho_{\mathrm{g}}/\mathrm{kg\cdot m^{-3}}$	Ar density	1.624
$\mu_{g}/\mathrm{Pa\cdot s}$	Ar viscosity coefficient	22.7×10^{-6}
$c_{pg}/\mathrm{J\cdot g^{-1}\cdot K^{-1}}$	Ar specific heat capacity	0.5215
$\rho/\mathrm{kg\cdot m^{-3}}$	Sn-20Bi-xIn density (x=0, 1, 2)	$7.65\times10^{3}/7.59\times10^{3}/7.53\times10^{3}$
$T_{\mathrm{S}}/°\mathrm{C}$	Sn-20Bi-xIn characteristic melting temperature (x=0, 1, 2)	186.3/182.2/177.1

$\Delta H/\mathrm{kJ}\cdot\mathrm{kg}^{-1}$	Latent Heat of Fusion of Sn20Bi-xIn (x=0, 1, 2)	36.5/30.7/24.8

Fig. 8(a) shows the evolution of the temperature field inside the droplet with falling distance. During the rapid cooling of the droplet, the droplet surface continuously dissipates heat to the surrounding environment, while a certain lag exists in the transfer of internal heat to the surface. The difference in heat transfer efficiency between the two leads to a faster cooling rate of the surface layer, whereas the internal heat of the droplet is difficult to conduct outward in time, and the temperature decrease in the central region lags relatively. Consequently, a radial temperature distribution trend of lower surface temperature and higher center temperature is formed. Fig. 8(b) shows the temperature and temperature gradient distributions of the sphere at a falling time of 0.1261 s, at which the sphere reaches its peak temperature. Through the model, the sphere is discretized radially into ten concentric annular grid cells, and the temperature gradient is obtained from the ratio of the difference between the surface temperature and the sub-surface temperature of the grid cell where the point is located to the radial distance:

$$G_i = \frac{|T_s - T_i|}{R - r_i} \tag{9}$$

where, G_i is the average radial temperature gradient between the surface and the i-th sub-surface, in ℃/m; T_s is the surface temperature of the sphere; T_i is the temperature at the i-th sub-surface position; and r_i is the radial distance from the i-th sub-surface position to the sphere center. Unlike the temperature distribution, the temperature gradient increases gradually from the center to the surface along the radial direction, that is, the closer to the surface, the faster the temperature decreases per unit distance. Owing to the geometric symmetry at the sphere center, the temperature variation near the center is relatively gentle, and the temperature gradient is small; whereas the region near the surface is more strongly affected by external convective and radiative cooling, and the temperature decrease per unit distance is more pronounced, resulting in a larger temperature gradient. This result indicates that during the solidification of the microsphere, heat is mainly transferred radially from the center to the surface, and the surface region exhibits a faster cooling response and may therefore reach the solidification condition earlier.

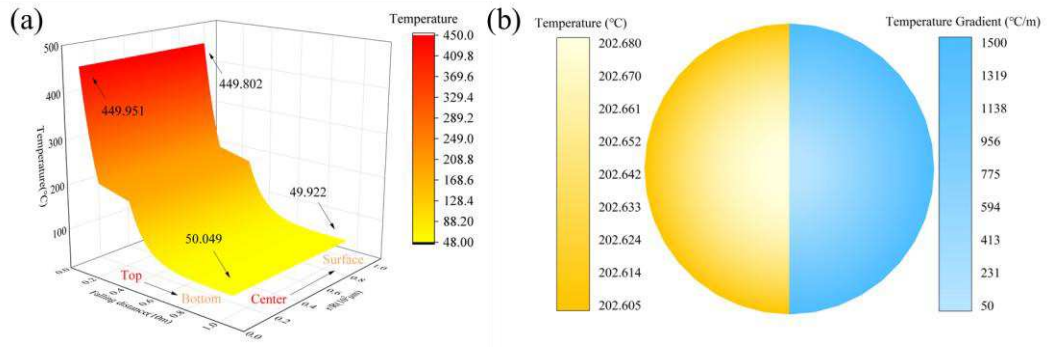


Fig. 8. Distribution of temperature of Sn20Bi microspheres versus reduced radial distance

r/R: (a) temperature field versus falling distance; (b) temperature (left) and temperature gradient (right) after falling for 0.1261 s.

As shown in Fig. 9(a), the dash-dotted line and the solid line represent the variations of the droplet center temperature T_C and surface temperature T_S with falling time, respectively. The cooling process of the droplet is jointly driven by external heat dissipation, internal heat conduction, and latent heat release during solidification, and its temperature evolution can be divided into three stages: liquid cooling, latent heat release during solidification, and solid-state cooling [34,35]. The first stage is the rapid cooling stage. Owing to the large temperature difference between the droplet and the surrounding argon gas, intense convective and radiative heat transfer causes the liquid metal to cool rapidly through sensible heat release, so the temperature curve exhibits a steep decline. The second stage is the latent heat release stage. When the temperature drops to near the liquidus and further undercooling occurs, solidification begins, accompanied by the formation of the primary Sn phase. During solidification, the released latent heat of crystallization partially offsets the heat dissipation from the droplet to the surroundings, significantly reducing the temperature decline rate [36]. The third stage is the late solidification and solid-state cooling stage. As the liquid volume fraction decreases, the latent heat release rate decreases, and the buffering effect of the temperature plateau gradually weakens, after which the droplet temperature rapidly decreases again.

The addition of In imparted a certain compositional dependence to the solidification behavior of Sn20Bi. In the model prediction, the solder balls containing 1 wt.% In entered the latent heat release and subsequent solidification stages earlier. In contrast, the sample containing 2 wt.% In exhibited a relatively delayed entry into the second stage and a correspondingly lower temperature; however, its transition from the second stage to the third stage was the most rapid, indicating that a higher In content accelerated the completion of the main solidification process. Overall, the addition of In did not change the fundamental trend of rapid cooling of the solder balls, but instead influenced their solidification process by regulating the cooling rate and solidification duration at different stages, thereby facilitating microstructural refinement and homogenization.

Fig. 9(b) shows the evolution of the radial temperature difference and cooling rate of the droplet with falling time. Here, the radial temperature difference is the difference between the center and surface temperatures of the droplet, and the cooling rate is calculated as the ratio of the surface temperature difference between adjacent moments to the time interval. The radial temperature difference reflects the degree of non-uniformity of the internal temperature field within the droplet, while the cooling rate reflects the rate of change of the droplet surface temperature with time. Both reflect the spatiotemporal variation characteristics of the temperature field during droplet cooling and may affect the solidification process [35].

In this study, the surface of the Sn20Bi microsphere first exchanges heat with argon and cools rapidly, while the temperature decrease in the central region lags relatively, thereby forming a radial temperature difference. When the surface cooling rate is relatively high, the droplet more readily establishes undercooling conditions and enters the nucleation and solidification stages; the variation in radial temperature difference reflects the degree of uniformity of the internal temperature field within the droplet during solidification. After the addition of 1 wt.% In, the total cooling time of the droplet was slightly shortened, the cooling rate in the solidification transition region was slightly increased, and the radial temperature difference was slightly reduced. Studies have shown that the addition of In can alter the thermal behavior, melting and solidification characteristics, and the

distribution of the Sn/Bi two-phase microstructure in Sn-Bi-based solders [11,12].

When the In content was increased to 2 wt.%, the radial temperature difference of the droplet increased slightly at the initial cooling stage, indicating that the degree of non-uniformity in the internal temperature response increased initially. As the cooling process proceeded, the radial temperature difference of this droplet gradually decreased, and the subsequent solidification stage had the shortest duration, indicating that the internal temperature difference of the droplet gradually diminished and that the main solidification transition stage predicted by the model was shortened in duration. Its effects on the partitioning of the Sn and Bi phases as well as the evolution of the residual Bi phase will be further analyzed in combination with the subsequent microstructural results.

Therefore, the addition of In did not simply alter the overall cooling rate of the droplet, but instead changed thermal history parameters such as the surface cooling rate, radial temperature difference, and duration of the solidification stage, thereby affecting the solidification process of the droplet.

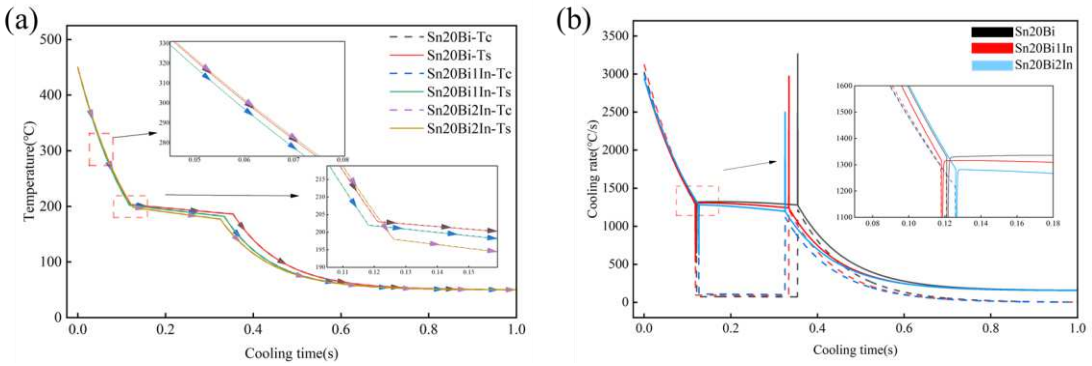


Fig. 9. Variations of temperature and cooling rate of Sn20Bi-xIn microspheres with time: (a) variations of center temperature and surface temperature with time; (b) variation curves of droplet surface cooling rate (dashed line) and radial temperature difference (solid line).

3.4 Characterization of Cross-sectional Microstructure

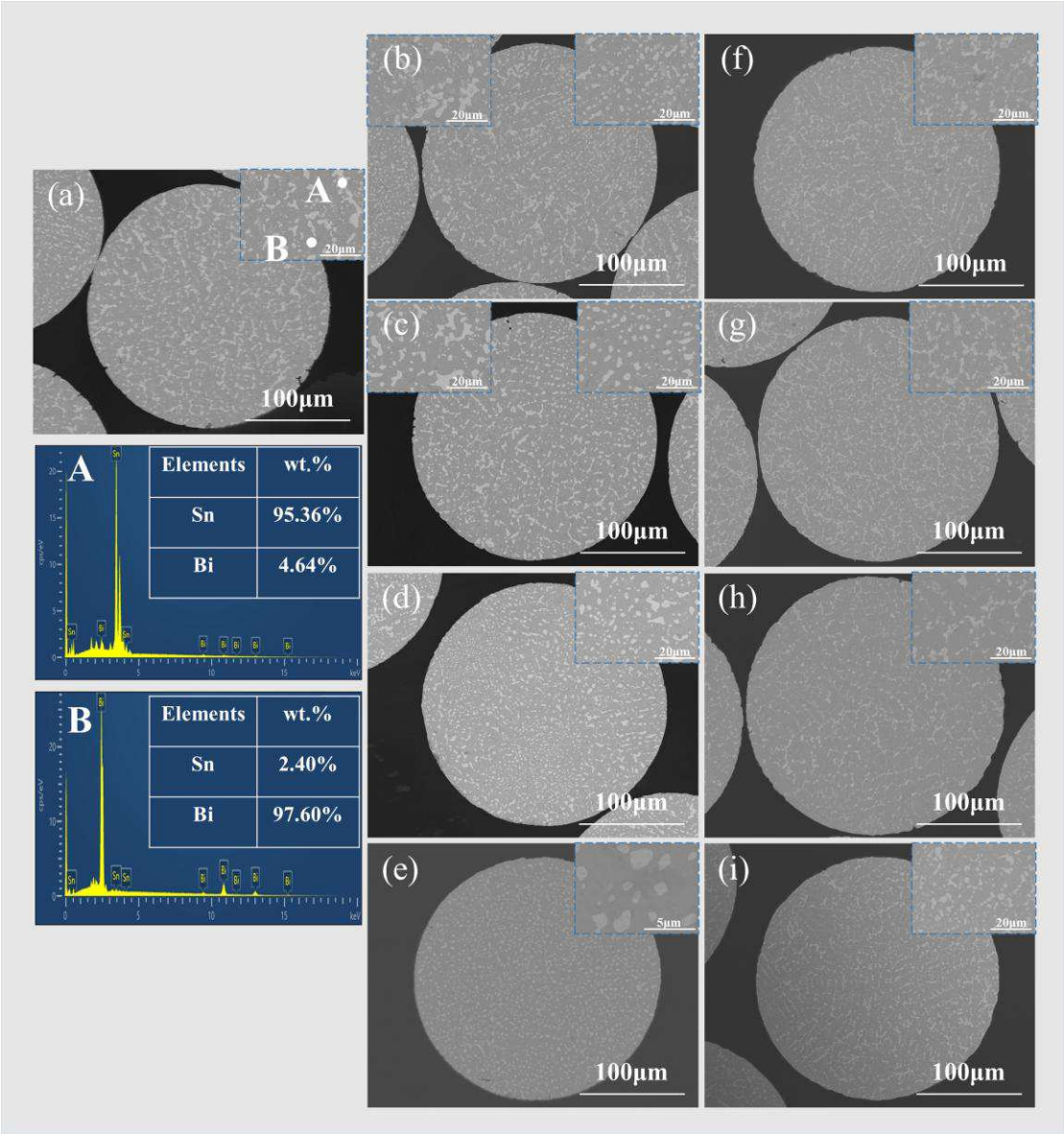


Fig. 10. Cross-sectional microstructures of the solder balls: (a) Sn20Bi; (b–e) Sn20Bi-xIn (x = 0.5–2 wt.%); (f–i) Sn20Bi-0.4Ni-xIn (x = 0.5–2 wt.%).

Fig. 10 shows the BSE images of the cross-sectional microstructures of Sn20Bi, Sn20Bi-xIn, and Sn20Bi-0.4Ni-xIn solder balls prepared by POEM, as well as the EDS point analysis results of Sn20Bi solder balls. As shown in Fig. 10(a), the cross-section of the solder ball exhibits an obvious two-phase microstructure. According to the EDS analysis results at points A and B, the gray region is the Sn-rich phase, while the white granular and short rod-like regions are the Bi-rich phase.

After the addition of In, the EDS elemental mapping results indicate that within the observed cross-sectional region, the Sn, Bi, and In elements are generally distributed relatively uniformly, with no obvious macroscopic elemental segregation. However, as can be seen from the SEM images,

certain differences exist in the size and morphology of the Bi-rich phase. As shown in Fig. 10(b) and (c), the Bi phase in some regions is relatively fine, while in other regions it exhibits larger island-like or rod-like morphologies. This difference may be related to the rapid solidification of the solder balls during cooling and solidification as well as the non-uniformity of the cooling rate within the droplet [37].

During droplet cooling, the β-Sn phase preferentially forms, while the Bi element gradually enriches into the remaining liquid phase. In regions with faster cooling, a larger local undercooling is more readily generated, which enhances the driving force for solidification nucleation and restricts the long-range diffusion of Sn/Bi atoms, thereby suppressing the coarsening of the Bi-rich phase. In contrast, in regions with relatively slower cooling or local accumulation of the Bi-rich liquid phase, larger island-like or short rod-like Bi phase structures are more readily formed.

When the In content was increased to 2 wt.%, as shown in Fig. 10(e), the Bi phase in the solder balls was significantly refined, indicating that the addition of 2 wt.% In markedly altered the solidification microstructural characteristics of the solder balls. Combined with existing studies, In can modify the melting and solidification characteristics and microstructural evolution behavior of Sn-Bi alloys [12,13], and may limit the coalescence and coarsening of the Bi-rich phase by affecting atomic diffusion processes, thereby promoting its refinement and dispersion. It should be noted that the specific effect of In on microstructural refinement may also be jointly related to the In content, local compositional distribution, and cooling conditions.

After the addition of Ni, the cross-sectional microstructure of the solder balls generally retained fine and uniform distribution characteristics, with the Bi phase mainly distributed in the Sn matrix in the form of fine granular, short rod-like, and discontinuous rod-like morphologies. Under the condition of a fixed addition of 0.4 wt.% Ni, the cross-sectional microstructures of solder balls with different In contents were generally similar, all exhibiting relatively uniform two-phase distribution characteristics. This may be related to the formation of the Ni_3Sn_4 second phase, which may provide heterogeneous nucleation sites and participate in the regulation of the solidification microstructure, thereby facilitating the refinement of the solidification microstructure. However, its specific effect on the coarsening behavior of the Bi-rich phase still requires further verification. Therefore, the addition of Ni is associated with the relatively fine characteristics of the solder balls.

3.5 Interfacial Reactions

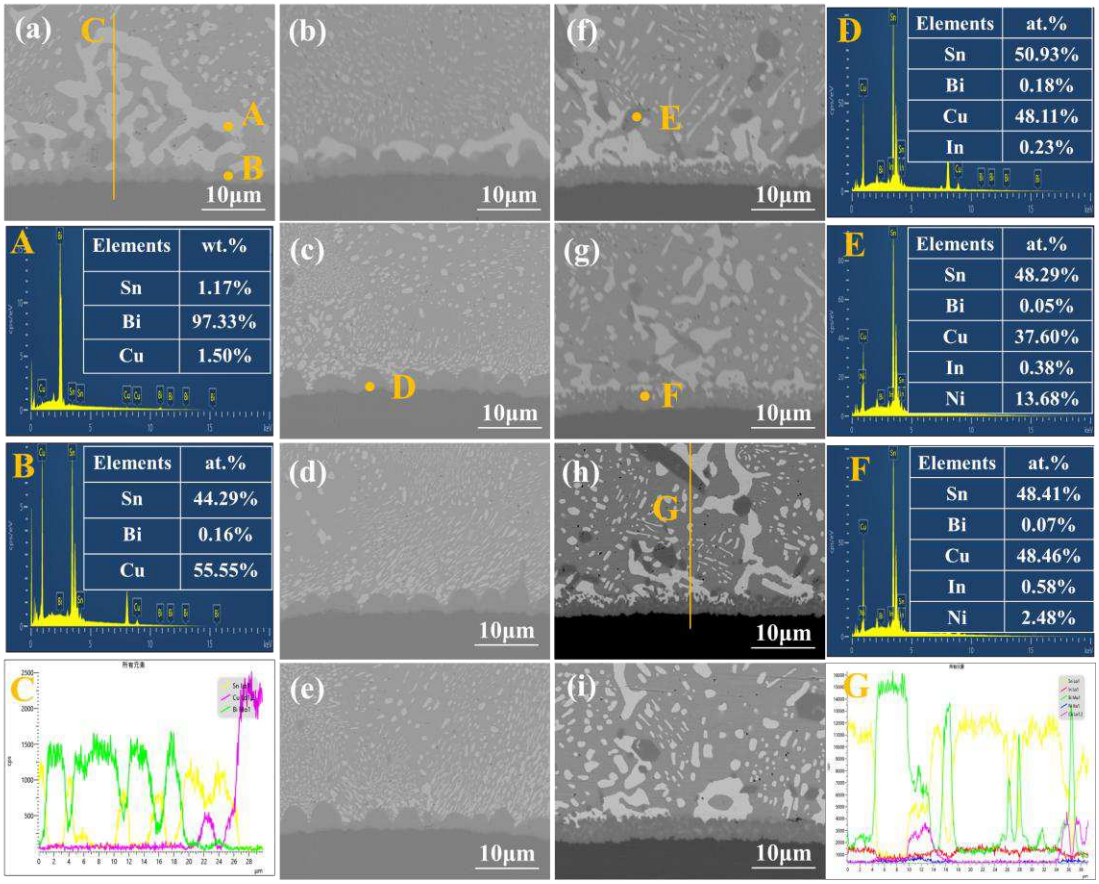


Fig. 11. Interfacial morphologies of IMCs: (a) Sn20Bi/Cu alloy; (b–e) Sn20Bi-xIn/Cu alloys; (f–i) Sn20Bi-0.4Ni-xIn/Cu alloys.

Fig. 11 shows the interfacial SEM morphology after the reaction between the solder balls and Cu pads. The results indicate that a reaction layer with an irregular undulating or scallop-like morphology formed at the interface. EDS point analysis of the solder ball matrix revealed that the white region (point A) is the Bi phase and the gray region (point B) is the Sn phase, while the line scan analysis along line C crossing both phases further confirmed the distribution characteristics of the two phases in the matrix; the interfacial IMC formed between the solder balls and Cu pads can be identified as Cu_6Sn_5. In Fig. 11(a), the Bi phase exhibits block-like, island-like, and locally continuous distribution within the solder ball and near the interface. This may be related to the consumption of Sn near the interface during the formation of Cu_6Sn_5 in the reflow process, which may lead to relative enrichment of Bi in the liquid phase near the interface [38], Since Bi is generally not the main reaction element for the formation of Cu-Sn interfacial IMCs, it may be enriched between the scallop-like Cu_6Sn_5 structures or near the interface, and form an observable Bi-rich phase during the subsequent cooling process.

Fig. 11(b)–(e) show that after the addition of In, the interfacial IMCs all maintained a typical scallop-like morphology. The EDS result at point D indicates that the interfacial reaction layer can be identified as $Cu_6(Sn,In)_5$ [13]. The addition of In may alter the interfacial reaction and IMC growth kinetics [39,40]: the DSC results (Fig. 7) show that under the same reflow temperature profile, the reduction in melting temperature by In may increase the time for which the solder balls remain

in the liquid phase during reflow, thereby possibly facilitating the interfacial reaction between the solder balls and Cu as well as the formation and growth of Cu_6Sn_5, and resulting in a typical scallop-like morphology. In addition, compared with the Sn20Bi solder joints without In addition, after the addition of In, the coarse block-like Bi-rich phase near the interface was significantly refined and tended to be dispersed, which may weaken the hindering effect of the Bi-rich phase on the local growth of Cu_6Sn_5, making the scallop-like morphology of the interfacial reaction layer more distinct.

Fig. 11(f)–(i) show that after further addition of Ni, the interfacial IMC evolved into a relatively thin, irregular continuous layer. EDS analysis (points E and F and line G) confirmed that the interfacial IMC can be identified as $(Cu,Ni)_6Sn_5$, and black rod-like Ni_3Sn_4 precipitates were observed. The addition of Ni is associated with changes in the morphology and thickness of the IMC layer, may alter its growth behavior, and may affect the brittle characteristics of the interface [41] [42].

In summary, the addition of In and Ni exerted different effects on the microstructure and reaction layer morphology of the Sn20Bi/Cu interface. In mainly manifested as a reduction in the characteristic melting temperature accompanied by refinement of the Bi-rich phase, thereby affecting the interfacial reaction; the addition of Ni was accompanied by the formation of Ni_3Sn_4 and the appearance of the $(Cu,Ni)_6Sn_5$ interfacial phase, and may alter the growth behavior of the IMC. The effects of the above changes in interfacial morphology and phase composition on the mechanical properties of the solder joints will be discussed in the subsequent shear tests.

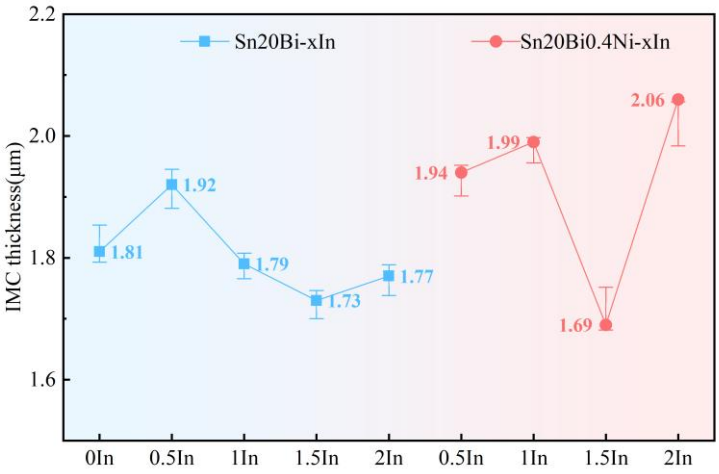


Fig. 12. Thickness of IMCs in Sn20Bi/Cu, Sn20Bi-xIn/Cu, and Sn20Bi-0.4Ni-xIn/Cu alloys.

Fig. 12 shows that the IMC layer of the Sn20Bi solder joints is not thick, which may be related to the regulation of the initial microstructure of the solder balls during the POEM preparation process. Since the droplets prepared by POEM undergo a rapid solidification process and are subjected to relatively consistent preparation and cooling conditions, the resulting solder balls possess uniform microstructural characteristics and a narrow size distribution, which facilitates the consistency of melting and spreading conditions of the solder balls during reflow. However, the IMC thickness cannot be used alone as the sole criterion for evaluating interfacial reliability. Previous studies have pointed out [39] that the formation of interfacial IMCs indicates that good metallurgical bonding has been established between the solder balls and the substrate, but IMC

phases generally exhibit relatively high brittleness, and their thickness and morphology can significantly affect the reliability of solder joints. For Sn20Bi solder joints, the relatively thin IMC layer may also be related to their poorer wettability and weaker degree of interfacial reaction. Since Bi generally does not directly participate in the formation of IMCs, the locally enriched coarse Bi phase may hinder effective contact between Sn and the Cu substrate, and may reduce the effective contact and reaction area between local Sn and Cu, thereby affecting the formation of the interfacial reaction layer and resulting in a relatively thin thickness [43]. After the addition of In, the characteristic melting temperature of the solder balls decreased, and the wettability was improved, enabling more sufficient contact with the pads, which may promote the interfacial reaction; therefore, the interfacial IMC layer exhibited a more continuous morphological feature. After further addition of Ni, the IMC thickness showed a non-monotonic trend with composition variation, indicating that the effect of Ni on the IMC layer is compositionally dependent, and its role is not simply to promote or inhibit IMC growth, but is jointly related to the In content, melting behavior of the solder balls, wetting and spreading ability, and interfacial diffusion process. Overall, In mainly promotes sufficient interfacial reaction by improving wetting and spreading and lowering the characteristic melting temperature, while Ni is accompanied by changes in the growth behavior of Cu_6Sn_5.

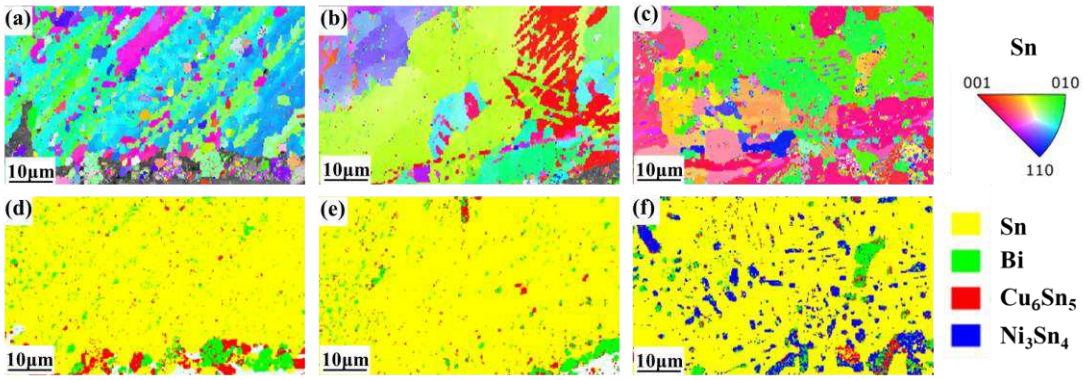


Fig. 13. IPF-x maps and phase composition maps of local regions of the solder matrix for Sn20Bi/Cu, Sn20Bi-1wt.%In/Cu, and Sn20Bi-0.4Ni-1wt.%In/Cu.

To further reveal the local microstructural evolution characteristics during the interfacial reaction, EBSD-IPF maps and phase maps were used to analyze local regions of the solder joints after reflow. Fig. 13 shows the orientation distribution results of the indexed phases in the local region. The IPF-x maps show that the size and distribution of continuous regions with the same orientation differ among samples with different compositions. Combined with the phase maps, it can be seen that some β-Sn regions in the Sn20Bi sample exhibit relatively continuous orientation characteristics. With the addition of In/Ni, the IPF color distribution and continuous orientation regions changed, indicating that the local crystallographic orientation distribution was regulated by microalloying. Since β-Sn exhibits pronounced crystallographic anisotropy, different grain orientations can lead to differences in the interfacial reaction of solder joints [44]. Therefore, the changes in local orientation distribution induced by microalloying may further affect the micromechanical behavior of the solder joints. The phase composition maps further indicate that the addition of In promoted the refinement of the Bi-rich phase, transforming it from a locally

aggregated state to a more uniform dispersed distribution. The Ni_3Sn_4 phase appeared in the Ni-containing samples and may participate in local microstructural regulation. Combined with their IPF-x maps, the introduction of the multiphase microstructure altered the local grain orientation and phase distribution characteristics, potentially affecting the local deformation behavior. Its effect on mechanical properties will be evaluated in combination with subsequent shear tests.

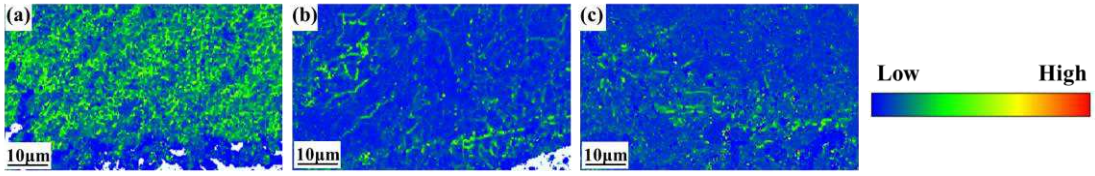


Fig. 14. KAM maps of local regions of the solder matrix for Sn20Bi/Cu, Sn20Bi-1wt.%In/Cu, and Sn20Bi0.4Ni-1wt.%In/Cu.

Based on the above analysis, it can be seen that microalloying affected the orientation distribution and multiphase microstructural state in local regions near the interface. To further reveal the influence of such local microstructural changes on the state related to lattice distortion, KAM maps were used for the analysis. In the Sn20Bi sample, green high-KAM regions were observed, indicating relatively large local orientation differences, which may be related to the non-uniform distribution of the coarse Bi phase. Owing to the differences in thermal expansion and mechanical properties between the coarse Bi phase and the Sn phase, relatively pronounced local lattice distortion may form near the phase boundaries during reflow cooling. After the addition of In, the green regions decreased, indicating that the local orientation gradient and the degree of lattice distortion were reduced, and the residual strain concentration was alleviated. Combined with the phase composition maps and SEM results, it can be seen that after In addition, the Bi phase was significantly refined and tended to be dispersed, which affects the local stress/strain and deformation behavior and is related to the improvement in shear strength in subsequent experiments [39]. After further addition of Ni on the basis of In, the KAM distribution became more uniform, and the local high-value regions further decreased, indicating that the local orientation difference in this sample was relatively small; the introduction of the second phase may be related to the KAM distribution [45]. Combined with the aforementioned IPF results, it can be seen that microalloying, while altering the local crystallographic orientation distribution, also reduced the local KAM level, indicating that the change in crystal orientation near the interface may help alleviate local lattice distortion and strain concentration.

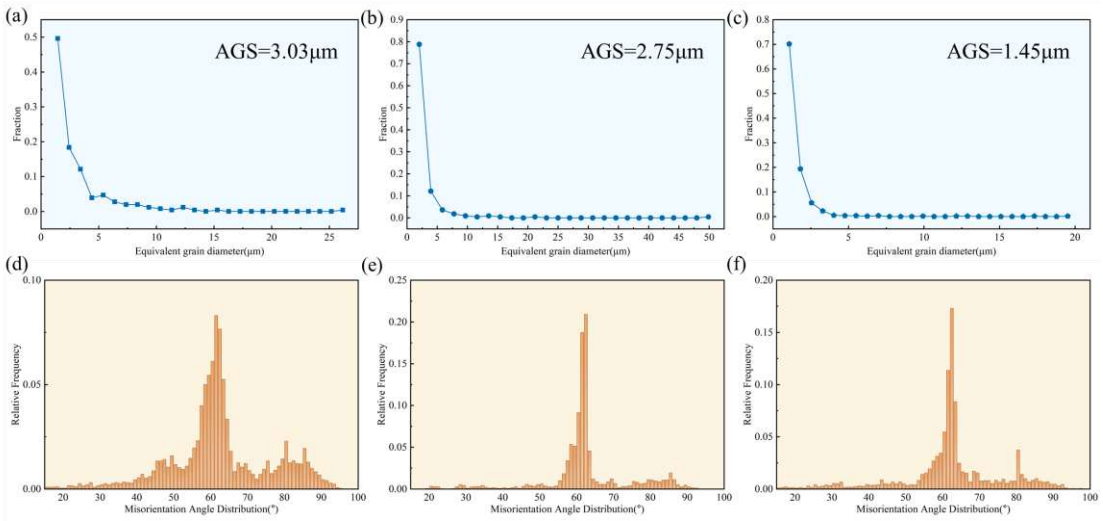


Fig. 15. Effective grain size (average grain size) distribution maps and misorientation angle distribution maps of Sn grains in local regions of the solder ball matrix for Sn20Bi/Cu, Sn20Bi-1wt.%In/Cu, and Sn20Bi-0.4Ni-1wt.%In/Cu.

To further analyze the effects of In and Ni on the β-Sn grain structure, the effective grain size and misorientation angle distribution in the EBSD data were statistically analyzed. The results are shown in Fig. 15, and the equivalent circle diameter formula used is as follows:

$$D_{eq} = 2\sqrt{\frac{A}{\pi}} \tag{10}$$

Where A is the grain area, and D_{eq} is the diameter of a circle with the same area as the grain. The effective grain size results show that with increasing In content, the average equivalent circle diameter of the β-Sn phase gradually decreased, indicating that In addition promoted Sn grain refinement [46]. After further addition of Ni, the sample exhibited the smallest equivalent grain size, and the Sn grain refinement effect was more pronounced among the compared samples. Meanwhile, with the gradual addition of In/Ni, the area-weighted average grain size decreased, consistent with the grain refinement trend. After microalloying, the local average equivalent grain size showed a decreasing trend, indicating that the scale of identifiable continuous-orientation grains in the EBSD-selected region decreased, and the degree of local microstructural subdivision increased. A misorientation angle of 15° was used as the grain boundary identification threshold to distinguish low-angle boundaries from high-angle boundaries, mainly reflecting the grain structure characteristics defined by high-angle grain boundaries. Related studies have found [39] that, in systems without Ni_3Sn_4 participating in nucleation, In addition can reduce the degree of dispersion of grain orientations in the matrix and promote the formation of preferred orientations related to {100}/{001}. The results indicate that after microalloying, the frequency of high-angle grain boundaries increased and exhibited a more pronounced concentrated distribution near specific misorientation angles, indicating that the β-Sn grains in the In+Ni sample were divided by more high-angle grain boundaries, and the orientation difference between grains was enhanced; combined with the IPF maps, the spatial correlation of same-orientation regions decreased, primarily reflecting

phase-boundary segmentation rather than an increase in intragranular orientation spread.The smaller β-Sn grain size and changes in high-angle grain boundary distribution may affect the local deformation behavior under shear loading and may alter the local slip and crack propagation paths. Overall, the EBSD results indicate that microalloying promoted local microstructural refinement and grain boundary reconstruction, and helped reduce the local orientation gradient and degree of lattice distortion. These changes may improve the shear strength of solder joints.

3.6 Wettability and Shear Properties

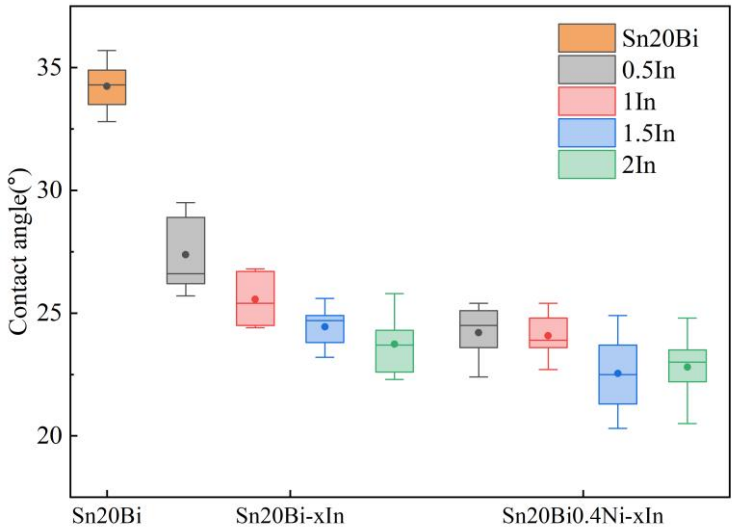


Fig. 16. Contact angles of Sn20Bi/Cu, Sn20Bi-xIn/Cu, and Sn20Bi-0.4Ni-xIn/Cu alloys.

Wettability is an important indicator for evaluating the spreading behavior of solder on substrate surfaces, and its variation is closely related to interfacial reactions and the state of joint formation. As a qualitative description of interfacial wetting behavior, wettability can be quantitatively characterized by the contact angle; the smaller the contact angle, the better the wettability. Under ideal equilibrium conditions, the contact angle is related to the solid-gas, solid-liquid, and liquid-gas interfacial energies. That is, the spreading behavior of molten solder on Cu pads is closely related to changes in the interfacial energies of the system, which can be described by Young's equation [47]:

$$\cos\theta = \frac{\gamma_{SV} - \gamma_{SL}}{\gamma_{LV}} \tag{11}$$

Where θ is the contact angle, γ_{SV} is the solid-gas interfacial energy,γ_{SL} is the solid-liquid interfacial energy, and γ_{LV} is the liquid-gas interfacial tension. The contact angle test results are shown in Fig. 16. The average contact angles of the solder balls in the various groups are 34.24°, 27.38°, 25.56°, 24.44°, 23.74°, 24.2°, 24.08°, 22.54°, and 22.8°. In the Sn20Bi-xIn series, the average contact angle of the solder balls gradually decreased with increasing In content; for the

Sn20Bi-0.4Ni-xIn series, the contact angle generally exhibited a decreasing trend, but the change was not monotonic. This phenomenon may be related to the effects of In on the melting behavior, interfacial state, and microstructural characteristics of the solder balls. On the one hand, the addition of In reduced the characteristic melting temperature of the solder balls, giving them a higher effective superheat under the same reflow conditions, which may facilitate the spreading of the solder on the Cu pad surface. On the other hand, previous studies have shown that a small amount of In can reduce the solid-liquid interfacial energy between the molten solder ball and the Cu substrate [12].According to Young's equation, when other interfacial energy conditions remain relatively stable, a decrease in γ_{SL} can increase $\cos\theta$ and decrease θ, thereby reducing the contact angle and improving wettability. After further addition of 0.4 wt.% Ni to the solder balls, the contact angles at the corresponding In contents generally showed little change, indicating that within the testing range of this study, the effect of Ni on the wetting behavior was relatively limited. A small amount of Ni_3Sn_4 may exert a certain influence on wettability by altering microstructural characteristics and interfacial reaction behavior [48].

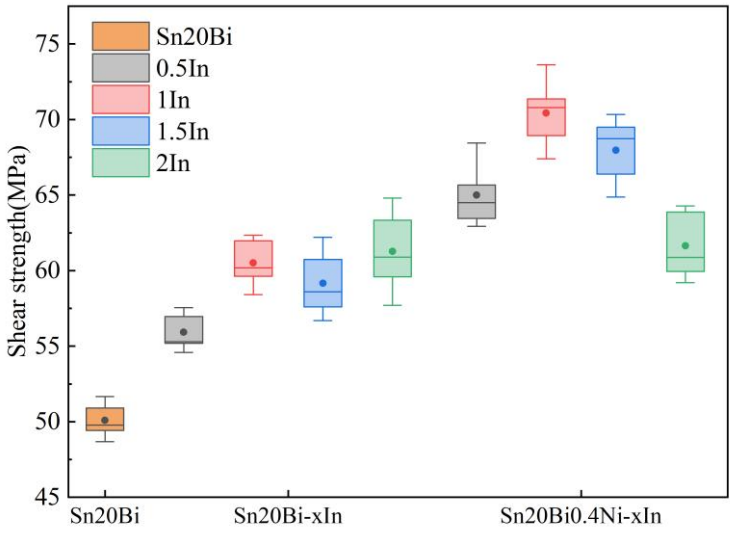


Fig. 17. Shear strength of Sn20Bi/Cu, Sn20Bi-xIn/Cu, and Sn20Bi-0.4Ni-xIn/Cu alloys.

Shear strength is an important indicator for evaluating the shear load-bearing capacity of solder joints and can be used to characterize the mechanical properties of solder joints under lateral loading. The ball shear test can characterize the shear load-bearing capacity of solder joints under lateral loading after solder ball reflow, and its results are jointly affected by factors such as the solder microstructure, interfacial IMC, and defect state. The results are shown in Fig. 17. The average shear strengths of the solder balls in the various groups are 50.09 MPa, 55.92 MPa, 60.51 MPa, 59.17 MPa, 61.27 MPa, 65.00 MPa, 70.42 MPa, 67.97 MPa, and 61.63 MPa. As shown in Fig. 17, the average shear strength of the Sn20Bi solder joints is 50.09 MPa, which is the lowest value among the samples tested in this study. With increasing In content, the shear strength of the solder joints generally exhibited an upward trend, but the change was not monotonic; compared with the Sn20Bi samples, the shear strength of the In-added samples was overall improved. Combined with the cross-sectional SEM and EBSD results, it can be seen that with the addition of In, the Bi phase transformed

from a coarse block-like/rod-like morphology to a fine and dispersed distribution, while the β-Sn grain size was generally reduced in the EBSD-characterized samples. The coarse Bi phase may cause local stress concentration under shear loading, whereas the refinement and dispersed distribution of the Bi phase help reduce local microstructural non-uniformity and may affect crack initiation and propagation behavior under shear loading [49]. In addition, In reduces the characteristic melting temperature of the solder balls and improves the wetting behavior, which may facilitate the formation of more sufficient interfacial bonding between the solder and the Cu substrate, thereby affecting the shear load-bearing capacity of the solder joints [50].

After further addition of 0.4 wt.% Ni, the Sn20Bi-0.4Ni-1In sample achieved the highest shear strength of 70.42 MPa; when the In content was further increased from 1 wt.% to 1.5 and 2 wt.%, the shear strength decreased to 67.97 and 61.63 MPa, respectively, but remained higher than that of the Sn20Bi sample. The above results indicate that the combination of In and 0.4 wt.% Ni affects the shear properties of Sn20Bi solder joints, but this effect is non-monotonic. On the one hand, a low In content can already effectively refine the Bi phase and improve wetting; on the other hand, Ni reacts with Sn to form Ni_3Sn_4, and previous studies have shown that Ni_3Sn_4 may participate in the refinement of the solidification microstructure and the second-phase strengthening process [16]. Meanwhile, after Ni addition, the composition and thickness of the interfacial IMC changed, and the β-Sn grain size was further reduced. Overall, the Sn20Bi-0.4Ni-1In sample exhibited a refined microstructural characteristic, good wettability, and the highest shear strength within the testing range of this study. When the In content was further increased, the shear strength of the solder joints decreased to some extent. This may be related to further changes in the microstructure and phase distribution at higher In contents, and its specific mechanism still requires further analysis in combination with results such as hardness and fracture morphology. In addition, the Ni_3Sn_4 second phase may also be affected by changes in the matrix microstructure and local phase distribution under high In conditions. Therefore, within the testing range of this study, the Sn20Bi-0.4Ni-1In sample exhibited the highest average shear strength, while further increasing the In content led to a decrease in shear strength, indicating that the In content has a non-monotonic effect on the shear properties of Sn20Bi-0.4Ni solder joints.

4.Conclusion

(1) In this study, high-precision and stable preparation of Sn20Bi, Sn20Bi-xIn, and Sn20Bi-0.4Ni-xIn solder balls was successfully achieved by POEM. After microalloying, the solder balls still maintained good spherical morphology and a relatively narrow particle size distribution, and the sphericity was generally improved. DSC results showed that with increasing In content, the characteristic melting temperature of the solder balls generally shifted toward lower temperatures; XRD results indicated that the solder balls were mainly composed of β-Sn and Bi-rich phases, and the Ni_3Sn_4 phase formed after Ni addition.

(2) Numerical simulations indicated that during droplet solidification in the POEM process, obvious center–surface temperature differences and radial temperature gradients existed, and the cooling rates of droplets with different compositions differed; the addition of In further regulated the droplet temperature distribution, radial temperature gradient, and cooling rate, thereby affecting the evolution of the solidification stage.

(3) In/Ni microalloying significantly improved the surface morphology and microstructure of Sn20Bi solder balls and induced changes in the interfacial microstructure and IMC characteristics of the solder ball/Cu interface. With increasing In content, the microsphere surface gradually became smooth, and the Bi-rich phase in the cross-section gradually transformed from a coarse block-like/rod-like morphology to a fine and dispersed distribution; after Ni addition, the microstructure overall exhibited a finer characteristic. After reflow soldering, Cu_6Sn_5 formed at the solder ball/Cu interface, and the minimum IMC layer thickness was 1.69 μm. EBSD results indicated that after microalloying, the β-Sn grain size decreased, the frequency of high-angle grain boundaries increased, and the grain orientation and local misorientation characteristics changed.

(4) The addition of In/Ni overall improved the wettability and shear load-bearing capacity of Sn20Bi solder joints. Sn20Bi-0.4Ni-1.5In had the minimum contact angle of 22.54°, and Sn20Bi-0.4Ni-1In had the highest shear strength of 70.42 MPa.

References

[1] H. Kang, S.H. Rajendran, J.P. Jung, Low melting temperature Sn-Bi solder: effect of alloying and nanoparticle addition on the microstructural, thermal, interfacial bonding, and mechanical characteristics. Metals 11, 364 (2021). https://doi.org/10.3390/met11020364

[2] M.F. Yu, W.W.M. Dai, Single-layer fanout routing and routability analysis for ball grid arrays. In 1995 IEEE/ACM International Conference on Computer-Aided Design (IEEE, Computer Soc Press, San Jose, Ca, 1995), pp. 581–586.

[3] W. Zhu, W. Zhang, W. Zhou, P. Wu, Improved microstructure and mechanical properties for SnBi solder alloy by addition of Cr powders. J. Alloy. Compd. 789, 805–813 (2019). https://doi.org/10.1016/j.jallcom.2019.03.027

[4] A.T. Avatare, R.E. Ustad, V.D. Chavan, Z.A. Sheikh, T.P. Kamble, L. Sajjad, G. Lee, S. Sabale, H. Kim, D. Kim, Recent challenges, advancements, and effects of nanoparticles on the low-temperature Sn-Bi solder alloys. Mater. Sci. Semicond. Process. 200, 110006 (2025). https://doi.org/10.1016/j.mssp.2025.110006

[5] K.-K. Xu, L. Zhang, L.-L. Gao, N. Jiang, L. Zhang, S.-J. Zhong, Review of microstructure and properties of low temperature lead-free solder in electronic packaging. Sci. Technol. Adv. Mater. 21, 689–711 (2020). https://doi.org/10.1080/14686996.2020.1824255

[6] C. Cai, Evaluation of reliability of low melting temperature Sn-Bi solder, English, State University of New York at Binghamton, 2022.

[7] W. Li, L. Mo, F. Chen, Z. Dai, Y. Xu, S. He, H. Nishikawa, Counter-intuitive mechanical performance variation in aged low-temperature interconnections in electronic packaging. Vacuum 227, 113367 (2024). https://doi.org/10.1016/j.vacuum.2024.113367

[8] Z. Lai, D. Ye, Microstructure and fracture behavior of non eutectic Sn-Bi solder alloys. J. Mater. Sci. -Mater. Electron. 27, 3182–3192 (2016). https://doi.org/10.1007/s10854-015-4143-4

[9] L.S. Kamaruzzaman, Y. Goh, Effects of alloying element on mechanical properties of Sn-Bi solder alloys: A review. Solder. Surf. Mt. Technol. 34, 300–318 (2022). https://doi.org/10.1108/SSMT-06-2021-0035

[10] A. Nabihah, M.S. Nurulakmal, Effect of In addition on microstructure, wettability and strength of SnCu solder. In Materials Today-Processings (Elsevier, Malaysia, 2019), pp. 803–809. https://doi.org/10.1016/j.matpr.2019.06.366

[11] B. Shen, S. Yang, M. Xu, J. Zhao, G. Liu, M. Xie, Q. Zhang, Effect of In addition on thermodynamic properties, wettability, interface microstructure, and soldering performance of SnBiAg-xIn/Cu solder joints. Metals 12, 1594 (2022). https://doi.org/10.3390/met12101594

[12] X. Chen, F. Xue, J. Zhou, Y. Yao, Effect of In on microstructure, thermodynamic characteristic and mechanical properties of Sn-Bi based lead-free solder. J. Alloy. Compd. 633, 377–383 (2015). https://doi.org/10.1016/j.jallcom.2015.01.219

[13] J.R. da S. Leal, R.A.V. Reyes, G.L. de Gouveia, F.G. Coury, J.E. Spinelli, Evaluation of solidification and interfacial reaction of Sn-bi and Sn-Bi-In solder alloys in copper and nickel interfaces. Metals 14, 963 (2024). https://doi.org/10.3390/met14090963

[14] O. Mokhtari, H. Nishikawa, Effects of In and Ni addition on microstructure of Sn-58Bi solder joint. J. Electron. Mater. 43, 4158–4170 (2014). https://doi.org/10.1007/s11664-014-3359-z

[15] A. Mishra, A. Kaushal, M.R. Kumar, Effect of Ci, Co, and Mn for the recent advancements and progress of Sn-X (X= Bi, Ag, Zn & Cu) solder alloys: A review. Microelectron. Reliab.

174, 115878 (2025). https://doi.org/10.1016/j.microrel.2025.115878
[16] W. Dong, J. Xu, F. Xu, Preparation of Sn20Bi-xNi solder balls by pulsated orifice ejection method and their micro joint properties. Powder Technol. 469, 121743 (2026). https://doi.org/10.1016/j.powtec.2025.121743
[17] K. Minagawa, Y.Z. Liu, H. Kakisawa, Y. Osawa, S. Takamori, K. Halada, Hybrid atomization process applied to fine lead-free solder powder production. Mater. Trans. 44, 1316–1319 (2003). https://doi.org/10.2320/matertrans.44.1316
[18] L. Li, T. Wang, W. Zhang, Fabrication of solder balls exceeding 1.00 mm via controlled cutting and remelting technology for electronic packaging materials. J. Electron. Mater. 55, 1086–1098 (2026). https://doi.org/10.1007/s11664-025-12472-8
[19] C.-Y. Huang, Y.-H. Lin, K.-C. Ying, C.-L. Ku, The solder paste printing process: Critical parameters, defect scenarios, specifications, and cost reduction. Solder. Surf. Mt. Technol. 23, 211–223 (2011). https://doi.org/10.1108/09540911111169057
[20] L. Wu, J. Luo, H. Tan, Y. Zhou, Y. Wang, Y. Dou, L. Qi, Bump morphology formation and transformation mechanism in solder droplet printing. Int. J. Mech. Sci. 306, 110826 (2025). https://doi.org/10.1016/j.ijmecsci.2025.110826
[21] Y. Lian, W. Dong, F. Xu, Microstructures and thermal properties of mono-sized Al-Si particles prepared by pulsated orifice ejection method. Mater. Charact. 221, 114774 (2025). https://doi.org/10.1016/j.matchar.2025.114774
[22] W. Dong, Z.R. Jia, X. Wang, F.M. Xu, Y. Zhao, Size-on-demand preparation of SAC305 solder balls based on pulsated orifice ejection method. Vacuum 217, 112522 (2023). https://doi.org/10.1016/j.vacuum.2023.112522
[23] Dong W., Liu S., Wang X., Xu, Research progress on the application of pulsated orifice ejection method. Materials reports. Mater. Rep. 39, 171–179 (2025).
[24] W. Dong, D. Liu, F. Xu, Performance characterization of Au-Ge solder ball bumps fabricated via the pulsated orifice ejection method. J. Mater. Res. Technol. 38, 2047–2057 (2025). https://doi.org/10.1016/j.jmrt.2025.08.042
[25] Y. Lin, R. Xu, Y. Qiao, N. Zhao, Effects of indium content on interfacial reaction and microstructure evolution of Cu/SAC-xIn/ENEPIG BGA solder joints. J. Mater. Sci. -Mater. Electron. 36, 812 (2025). https://doi.org/10.1007/s10854-025-14865-1
[26] P. Peng, Analysis on the growth and growth-dependent microhardness of Ni3Sn4 intermetallic compound phase in directionally solidified Sn-Ni alloy. J. Alloy. Compd. 821, 153397 (2020). https://doi.org/10.1016/j.jallcom.2019.153397
[27] X.-L. Tang, Z.-H. Ge, Z. Li, K. Zhao, Enhanced thermoelectric properties of Ca3Co4O9+δ ceramics by Sr substitution. Solid State Sci. 104, 106190 (2020). https://doi.org/10.1016/j.solidstatesciences.2020.106190
[28] X. Kong, Z. Liu, R. Ma, J. Zhai, Z. Pan, X. Li, F. Sun, Microstructural and mechanical responses of Sn58Bi/Cu composite solder joints with 0.1wt.% Ni and carbon fiber addition. Sci. Rep. 14, 32141 (2024). https://doi.org/10.1038/s41598-024-83905-3
[29] N.X. Ho, T. V. Yen, T. V. Vu, Multiple drops solidifying on a surface with a temperature gradient. Eur. J. Mech. B-Fluids 111, 113–119 (2025). https://doi.org/10.1016/j.euromechflu.2024.12.009
[30] J. Qin, W. Zhu, M. Yu, R. Li, X. Zhang, Effects of cooling condition and strain rate on mechanical properties of SnBi36Ag0.5 alloy. Electron. Compon. Mater. 41, 514–519 (2022).

https://doi.org/10.14106/j.cnki.1001-2028.2022.1626
[31] J. Chen, S. Tang, Q. Cheng, M. Yao, W. Dong, X. Wang, Heat transfer mechanisms for micron-sized pure metal spherical particles during containerless solidification process. Appl. Therm. Eng. 283, 128883 (2026). https://doi.org/10.1016/j.applthermaleng.2025.128883
[32] S. Tang, Y. Yue, Z. Wang, M. Yao, W. Dong, X. Wang, Numerical modelling and simulation of heat transfer for micro-sized spherical Al-4.5 wt% Cu alloy particles. Appl. Therm. Eng. 258, 124845 (2025). https://doi.org/10.1016/j.applthermaleng.2024.124825
[33] X. Wang, P. Li, S. Tang, M. Yao, W. Dong, Simulation on heat transfer and solidification behavior of micron-sized Cu spherical particles prepared by pulsated orifice ejection method. Rare Metal Mat. Eng. 53, 124–134 (2024). https://doi.org/10.12442/j.issn.1002-185X.20220987
[34] Y.H. Su, C.-Y.A. Tsao, Modeling of solidification of molten metal droplet during atomization. Metall. Mater. Trans. B-Proc. Metall. Mater. Proc. Sci. 28, 1249–1255 (1997).
[35] K.-C. Chang, C.-M. Chen, Revisiting heat transfer analysis for rapid solidification of metal droplets. Int. J. Heat Mass Transf. 44, 1573–1583 (2001). https://doi.org/10.1016/S0017-9310(00)00193-9
[36] E.M.A. Ahmed, M.A. Amin, N.I.A.A. Tubaylah, Evolution of microstructure and physical properties of lead-free Sn–5Sb-Ag rapidly solidified solder alloys. Appl. Phys. A-Mater. Sci. Process. 127, 403 (2021). https://doi.org/10.1007/s00339-021-04539-0
[37] X. Wang, C. Li, Y. Xu, Y. Li, Revisiting the vacancy diffusion behavior under the influence of solute trapping in dilute alloys. Acta Mater. 288, 120788 (2025). https://doi.org/10.1016/j.actamat.2025.120788
[38] S. Ouyang, Z. Li, M. Bao, Y. Cao, Guoqi Hu, X. Xu, Interfacial reaction and mechanical properties of Sn–Bi Cu core solder joints. J. Mater. Res. Technol. 33, 7274–7283 (2024). https://doi.org/10.1016/j.jmrt.2024.11.109
[39] W. Wang, L. Sun, P. He, L. Zhang, J. Li, S. Zhang, Effect of indium (In) on the microstructure evolution, grain orientation and mechanical behaviors of Sn58Bi/Cu solder joints under thermal cycling. Mater. Charact. 229, 115608 (2025). https://doi.org/10.1016/j.matchar.2025.115608
[40] S. Zhang, W. Long, P. Li, F. Liu, H. Xue, T. Ding, Low-temperature lead-free SnBiIn solder for electronic packaging. J. Mater. Sci. -Mater. Electron. 35, 690 (2024). https://doi.org/10.1007/s10854-024-12405-x
[41] Z. Min, Y. Qiu, Interfacial reaction and IMCs formation between Sn-0.7Cu solder and Cu substrate during reflow soldering. In 16th International Conference on Electronic Packaging Technology, ICEPT 2015, August 11, 2015 - August 14, 2015 (Institute of Electrical and Electronics Engineers Inc., Changsha, China, 2015), pp. 1367–1370. https://doi.org/10.1109/ICEPT.2015.7236833
[42] B. Wang, J. Zhao, Y. Xiang, Q. He, F. Li, S. Zhang, J. Wang, J. Yan, The synergistic inhibition of the growth of intermetallic compounds at SAC305/Cu interface by Ni and Bi. Mater. Charact. 232, 116024 (2026). https://doi.org/10.1016/j.matchar.2026.116024
[43] F. Wang, Y. Huang, Z. Zhang, C. Yan, Interfacial reaction and mechanical properties of Sn-Bi solder joints. Materials 10, 920 (2017). https://doi.org/10.3390/ma10080920
[44] W. Zhao, K. Zhang, Y. Zhang, Z. Liu, H. Zhang, C. Zhang, Effect of Sn grain orientation on microstructure and mechanical properties of pure Sn solder joints under thermoelectric

coupling. Sci. Rep. 15, 27375 (2025). https://doi.org/10.1038/s41598-025-12625-z
[45] C. Chen, L. Zhang, X. Wang, X. Lu, L. Gao, M. Zhao, Y. Guo, Mechanical properties and microstructure evolution of Cu/Sn58Bi/Cu solder joint reinforced by B4C nanoparticles. J. Mater. Res. Technol. 23, 1225–1238 (2023). https://doi.org/10.1016/j.jmrt.2023.01.077
[46] X.L. Ren, X.Y. Liu, S.Y. Shi, Y.P. Wang, N. Zhao, Morphologies and nucleus models of β-Sn grains in SAC305-xIn freestanding solder balls and solder joints. Mater. Charact. 199, 112847 (2023). https://doi.org/10.1016/j.matchar.2023.112847
[47] L. Zang, Z. Yuan, H. Zhao, X. Zhang, Wettability of molten Sn-Bi-Cu solder on Cu substrate. Mater. Lett. 63, 2067–2069 (2009). https://doi.org/10.1016/j.matlet.2009.06.052
[48] Q. Song, Y. Li, J. Yu, D. Qi, W. Qin, Y. Zhan, Effect of Ni and TiO2 particle addition on the wettability and interfacial reaction of Sn20Bi lead-free solder. J. Mater. Sci. -Mater. Electron. 33, 3306–3319 (2022). https://doi.org/10.1007/s10854-021-07531-9
[49] J. Shen, Y. Pu, H. Yin, D. Luo, J. Chen, Effects of minor Cu and Zn additions on the thermal, microstructure and tensile properties of Sn-Bi-based solder alloys. J. Alloy. Compd. 614, 63–70 (2014). https://doi.org/10.1016/j.jallcom.2014.06.015
[50] E.E.M. Noor, N.M. Sharif, C.K. Yew, T. Ariga, A.B. Ismail, Z. Hussain, Wettability and strength of In-Bi-Sn lead-free solder alloy on copper substrate. J. Alloy. Compd. 507, 290–296 (2010). https://doi.org/10.1016/j.jallcom.2010.07.182